

Functional Materials for Information and Energy Technology: Insights by Photoelectron Spectroscopy

Martina Müller^{a,b,c}, Slavomir Nemsak^{a,b}, Lukasz Plucinski^{a,b}, Claus M. Schneider^{a,b,c}

^aPeter Grünberg Institut (PGI-6), Forschungszentrum Jülich, 52425 Jülich, Germany

^bJARA Jülich-Aachen Research Alliance, Forschungszentrum Jülich, 52425 Jülich, Germany

^cFakultät für Physik, Universität Duisburg-Essen, 47048 Duisburg, Germany

Abstract

The evolution of both information and energy technology is intimately connected to complex condensed matter systems, the properties of which are determined by electronic and chemical interactions and processes on a broad range of length and time scales. Dedicated photoelectron spectroscopy and spectromicroscopy experiments can provide important insights. We discuss some recent methodological developments with application to relevant questions in spintronics, and towards the in-operando studies resistive switching and electrochemical processes.

1. Introduction

The development of modern technology relies strongly on advanced condensed matter systems, for example, complex layered structures. The specific functionality of a layer stack is often determined by both the layer sequence and the interfaces between adjacent layers. This holds for many systems discussed in the context of information technology, such as nano- and spin electronics, but also in devices developed for energy harvesting, conversion and storage, such as photovoltaic cells, fuel cells or advanced batteries.

Common to all of the above cases is the challenge to disentangle the electronic structure and chemical states in the individual constituents and interfaces in a layer stack. Moreover, there is the desire to follow the evolution of an electronic or chemical signature *in operando*, i.e. during the operation of a specific device. This may include switching processes of state variables in memory cells, charge separation in photovoltaic elements, or redox processes in electrochemical cells.

Photoelectron spectroscopy (PES) is a very versatile tool for the investigation of electronic and chemical states [1–3]. The recent years have seen several advances which further increase the capabilities of PES. The limited information depth at soft x-ray excitation (XPS) can be overcome by exciting the photoelectrons with hard x-rays up to 10 keV [4, 5]. The x-ray standing wave approach provides access to specific spectroscopic information from buried interfaces [6]. The evolution in spectrometer design enables XPS experiments at near ambient pressure ($\lesssim 15$ mbar) [7, 8] or with lateral resolution in the sub-100 nm regime [9, 10]. The latter spectromicroscopy concept has been successfully extended to the hard x-ray regime [11, 12].

In the following we will discuss some applications of advanced photoemission spectroscopy and spectromicroscopy

techniques with soft and hard x-rays to material systems relevant for information technology and energy science.

2. Angle-Resolved Hard X-Ray Photoemission

Angle-resolved photoelectron spectroscopy (ARPES) has been the method of choice to investigate the electronic band structure of crystalline surfaces and novel electronic materials. Traditional ARPES employs VUV photons (20–150 eV) which in case of valence bands translates into similar kinetic energies of the emitted electrons. The inelastic mean free path (IMFP) of such electrons is $\lambda_{in} < 1$ nm, translating into a surface sensitivity, which is one of the key advantages of ARPES. On the downside, however, it obscures the access to the true bulk electron dispersion and to electronic states localized at buried interfaces.

One way of increasing λ_{in} and thus the probing depth of the ARPES experiment, is to employ low photon energies (i.e. below $h\nu = 10$ eV), however, this is material dependent, and the kinetic energy must be in any case larger than the work function W_F (for most surfaces W_F is around 4 to 5 eV). Therefore, the only safe way to increase λ_{in} is to perform HARPEs (hard X-ray ARPES) experiments at photon energies in the multi-keV regime.

Since λ_{in} should increase approximately as $E_k^{0.75}$, one can reach $\lambda_{in} \sim 30 - 60$ Å at 3-6 keV excitation energies. In addition a greater probing depth decreases the smearing in electron momentum perpendicular to the surface, which is proportional to $1/\lambda_{in}$ via the uncertainty principle.

Nevertheless, phonon effects set a fundamental limit of the momentum resolution of the HARPEs experiment. At high temperatures signatures of the band dispersions fade out in $E(\vec{k})$ maps, and the valence band photocurrent reaches the matrix-element weighted density-of-states limit (MEWDOS, also often termed the XPS limit), typically also modulated by X-ray photoelectron diffraction

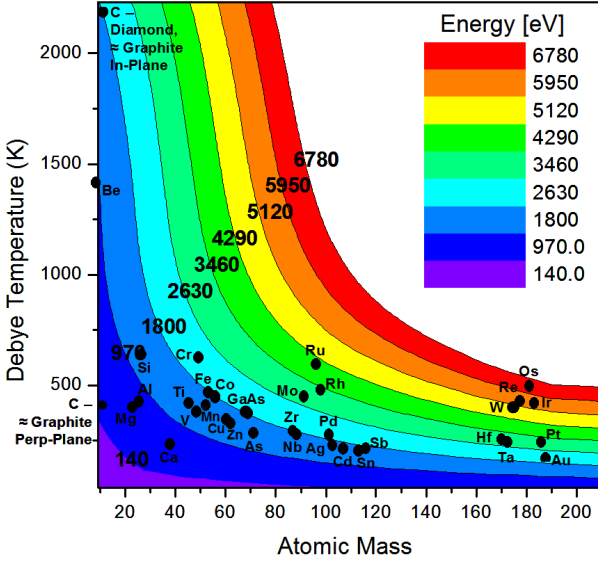


Figure 1: Kinetic energies for 0.5 DW factor for various elements.

effect [13]. Fraction of direct transitions can be estimated from the temperature-dependent Debye-Waller factor $W(T) \approx \exp(-g^2 \langle u^2(T) \rangle)$, where \vec{g} is the reciprocal lattice vector to allow direct transition, i.e. first Brillouin zone folding, and $\langle u^2(T) \rangle$ is the one-dimensional mean-squared vibrational displacement at temperature T . One can set $W = 0.5$ as a rather arbitrary limit at which realistic ARPES band mapping can be performed, and Fig. 1 shows $W(T)$ contours at 20 K for selected elements [14]. There one can see, that band mapping at up to 2 keV is possible for most elements, however, this is in most cases conservative, since clear signatures of dispersions can also be clearly observed for lower W values, when suitable corrections for non-dispersive densities of states and photoelectron diffraction are applied to ARPES maps of suitable signal to noise ratio. Realistic simulations of the temperature-dependent HARPES spectra have been recently performed using the one-step photoemission formalism [15].

Another effect which cannot be neglected at the multi-keV energy range is the photoelectron energy loss due atomic recoil when the highly-energetic electron leaves [16, 17].

The effect of temperature broadening is illustrated in Fig. 2(a-b). These results were obtained at $h\nu=6$ keV, which translates into 50-60 Å probing depth, a true bulk sensitive band mapping. $E(k)$ maps were measured on W(110) surface at room temperature and at 30 K are presented [22]. Debye-Waller factor for tungsten at 300 K is $W = 0.09$, therefore the room temperature spectrum in Fig. 2(a) shows the MEWDOS limit. At 30 K the Debye-Waller factor $W = 0.45$ and in Fig. 2(b) one can clearly see the signatures of tungsten bulk band dispersion.

At kinetic energies above ≈ 500 eV the final state of photoemission experiment can be approximated by free-electron parabola according to $E_f(k_f) = \hbar^2 k_f^2 / (2m_e)$, which

allows for convenient interpretation of the measured valence band dispersions as long as they can be well approximated by state-of-the-art *ab-initio* calculations. Such interpretation is presented in Fig. 2(c), where free-electron final-state simulations (based on a state-of-the-art density functional theory (DFT) with generalized gradient approximation (GGA)) ground state band dispersions are found to be in a very good agreement with measured bands. Photon momentum $k_{k\nu} = 2\pi\nu/c$, which is normally neglected in VUV ARPES, at multi-keV excitations reaches values comparable to the size of the Brillouin zone of a typical crystal. This is illustrated in Fig. 2(d), where photon momentum equals approximately the size of the entire Brillouin zone.

3. Spintronics: Dilute Magnetic Semiconductors

Recent years have witnessed a tremendous success of silicon spintronics, with considerable efforts being invested to realize applications such as e.g. a spin transistor [18]. One of the most important prerequisites for their operation is an efficient spin injection/detection into Silicon, the platform of contemporary electronics. Thereby, spin source/drain contacts need to meet two basic requirements: firstly, they must generate highly spin-polarized electron currents and, secondly, interface the semiconductor with smallest possible conductance mismatch. Various ferromagnetic 3d transition or half-metals have been investigated as spin-polarized source/drain materials, whereat inserting a tunnel barrier in between the silicon and metal electrode has turned out to be mandatory to ensure their spin-dependent electrical matching. Another option for the ferromagnetic electrode material comprises dilute magnetic semiconductors (DMS). However, DMS are hampered by low magnetic ordering temperatures T_C . A prominent dilute magnetic semiconductor is Mn-doped GaAs [19]. Despite being successfully used in spin electronic devices [20], the microscopic origin of the ferromagnetism in GaMnAs is still disputed.

Figure 3 illustrates the application of HARPES method to unravel the nature of ferromagnetism in the dilute magnetic semiconductor GaMnAs [21]. In such ternary disordered alloy, where some Ga sites are substituted by Mn, preparation of the stoichiometric surface is very challenging, and magnetic properties of such surface might be significantly different than bulk properties. Figure 3(a-b) shows HARPES $E(k)$ for pure GaAs and $\text{Ga}_{0.97}\text{Mn}_{0.03}\text{As}$, where clear broadening of most of the spectral features is observed. However, spectra are not only broadened, but also positions and shapes of important spectral features change between GaAs and $\text{Ga}_{0.97}\text{Mn}_{0.03}\text{As}$, as shown in Fig. 3(c). Such semi-quantitative analysis is possible because of the increased probing depth at high energies, which allows neglecting the spectral contribution related to the preparation-dependent surface cleanness. Figure 3(d) shows the magnified region near the valence band maximum, which indicates the existence of the Mn-related fea-

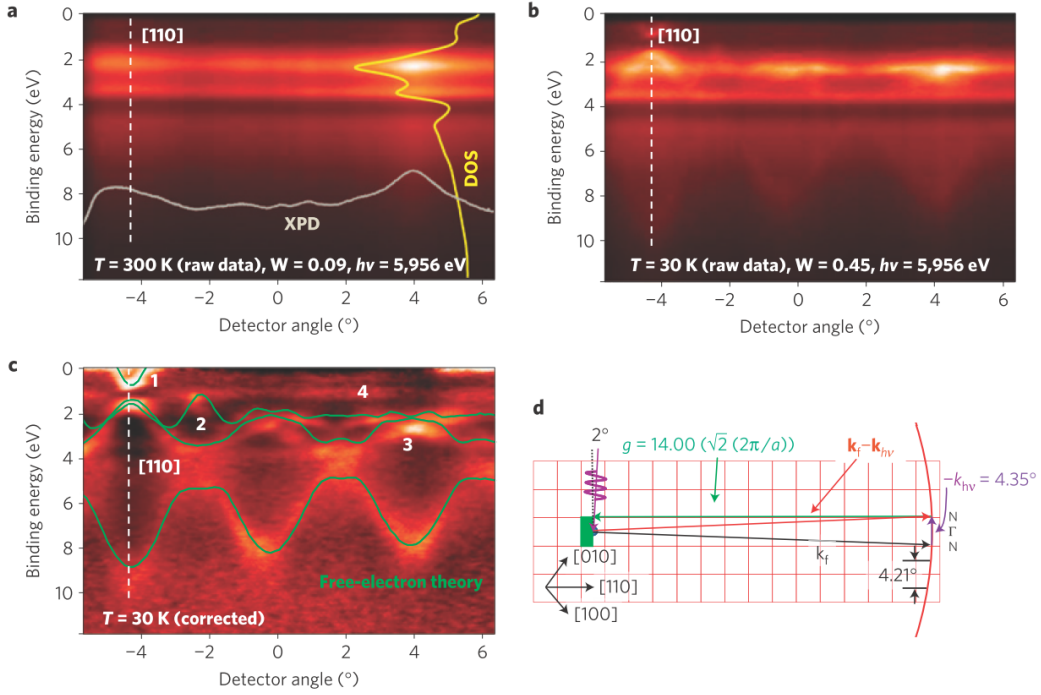


Figure 2: Figure showing the effect of phonon broadening and DW factor interpretation. Furthermore one can discuss photon momentum and related broadening due to large \vec{G} .

ture 400 meV below the Fermi level in $\text{Ga}_{0.97}\text{Mn}_{0.03}\text{As}$, which plays a crucial role in the interpretation of origin of ferromagnetism in this material. There is no gap between this feature and the mainly GaAs-derived valence band, which suggests that magnetism originates from the coexistence of the two mechanisms – double exchange and $p-d$ exchange, as suggested by theoretical models [23].

Add something on standing wave + HAPRES.

4. Spintronics: Magnetic Tunneling Barriers

To date the effectiveness of spin injection/detection is still mediocre, and hence a major advancement in this field is the integration of functional materials which combine the ability to generate highest spin polarization with a negligible conductivity mismatch. Magnetic oxides have recently re-emerged as highly effective spin filter materials [24, 25], and hence their integration as magnetic tunnel barriers with Silicon is of utmost interest [26]. Europium (II) oxide is widely considered as the most promising ferromagnetic oxide for silicon spintronics, because it has been shown to generate $> 90\%$ current spin polarization via the spin filter tunneling effect and is predicted to be thermodynamically stable in direct contact with silicon [27]. However, combining an ionic with a covalent material with large lattice mismatch poses a number of experimental challenges. In particular, the control of the EuO/Silicon interface is essential to avoid the formation of metallic impurity phases, in order to enable an effective spin transport from the magnetic tunnel barrier into the Si electrode. Fi-

nally, stabilizing ferromagnetic, divalent Eu(II)O itself is an experimental challenge due to its metastable oxidation state in ambient atmosphere.

We have succeeded in synthesizing high quality EuO/Si heterostructures and studied the EuO ultrathin film and EuO/Si interface properties with regard to their applicability as magnetic tunnel contacts. The growth of EuO/Si heterostructure was carried out as a two-step procedure, involving an initial chemical treatment of the Si(001) surface by either wet HF etching or by a passivation of ultrathin SiO_2 , followed by reactive Eu:O synthesis using the Eu distillation condition under UHV conditions and elevated substrate temperature [28]. We fabricated ultrathin EuO films ($d = 45\text{\AA}$) with two different compositions, i.e. stoichiometric Eu(II)O and oxygen-rich Eu(II,III), by supplying an oxygen partial pressure between $p_{\text{O}_2} = 2 - 4 \times 10^{-9}$ Torr. Further experimental details are given in Refs. [30, 31].

Hard X-ray photoemission spectroscopy (HAXPES) was used to probe the electronic structure of EuO magnetic tunnel barriers and the EuO/Si interface. Due to its large information depth exceeding 10 nm at photon energies of 10 keV, HAXPES is a perfect tool to probe the electronic structure of interfaces and buried layer [32]. Experiments were carried out at the beamline P09 at PETRAIII (DESY Hamburg, Germany) [33] and at the KMC-1 dipole beamline at BESSY II (Berlin, Germany) [34] with the HIKE endstation, featuring a total energy resolution of ~ 0.5 eV for $h\nu = 4$ keV.

First, we demonstrate that stabilizing high-quality EuO

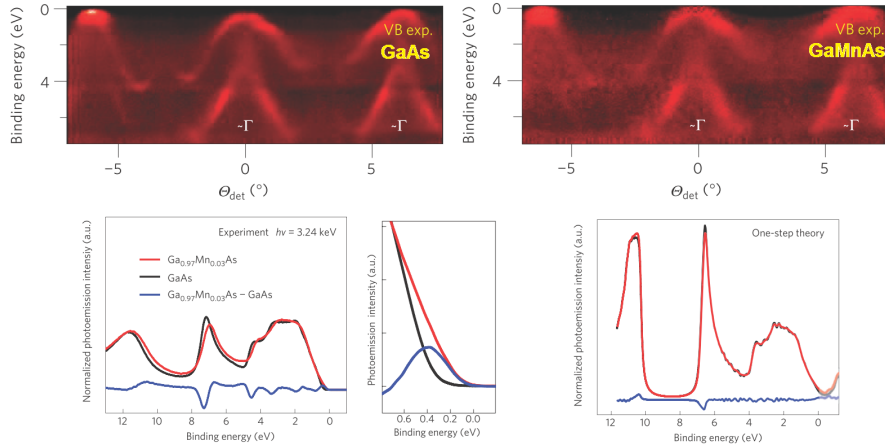


Figure 3: Figure showing HARPES spectra of GaAs and GaMnAs.

directly on Silicon is feasible within a narrow range of optimized synthesis parameters. Fig. 4 shows the Eu 4s and Eu 4d core level spectra for (a),(b) stoichiometric Eu(II)O and (c),(d) oxygen-rich Eu(II, III). For the Eu 4s levels in Fig. 4 (a) and (c), the clear double-peak structure is caused by coupling of the 4s core-level electrons with the localized Eu 4f state, which leads to an exchange splitting $\Delta E = 7.4$ eV of the 4s inner shell. The spins in the 4s photoemission final state $4s^1 4f^7$ are predicted to antiparallel (low spin, 7S) for the lower binding energy peak and parallel (high spin, 9S) for the higher binding energy peak with respect to the 4s emitted spin. For stoichiometric EuO, the 4s double-peak in Fig. 4 (a) is assigned to divalent Eu^{2+} spectral contributions, whereas an additional overlapping double-peak feature appears in Fig. 4 (c), which is chemically shifted by 8.1 eV towards higher binding energy and corresponds to trivalent Eu^{3+} cations.

Due to the strong $4d - 4f$ exchange interaction and much weaker $4d$ spin-orbit splitting, the prominent Eu 4d double peak structures in Fig. 4 (b) and (d) are assigned to a $J = L - S$ multiplet splitting, and the two peaks are denoted as 7D_J and 9D_J multiplets [37], respectively. The fine structure of the 7D final state is not resolved, whereas the $J = 2 - 6$ components in the 9D state are easily identified. We clearly observe a mainly divalent Eu^{2+} valency in Fig. 4 (b), but significant spectral contributions from trivalent Eu^{3+} cations in oxygen-rich EuO in Fig. 4 (d).

For both sample types, stoichiometric Eu(II)O and oxygen-rich Eu(II,III)O, we performed SQUID measurements as shown in Fig. 5(c). In stoichiometric Eu(II)O, the $M(T)$ characteristics roughly follows a Brillouin function with $S = 7/2$. A Curie temperature T_C of 66 K and a magnetic saturation moment of $M_S = 6.7\mu_B$ is observed, closely matching the bulk values of 69 K and $7\mu_B$ per Eu^{2+} , respectively. The $M(H)$ characteristics recorded at $T = 2$ K (see inset of Fig. 4(c)) displays a square-like FM hysteresis with a relatively small coercive field of $H_c = 100$ Oe. In contrast, the sample comprising oxygen-rich Eu(II,III)O reveals a $M(T)$ curve which is almost completely sup-

pressed. Here, a reduced magnetic saturation moment $M_S = 1.5\mu_B$ is detected at $T = 2$ K, caused by paramagnetic Eu^{3+} cations in Eu_3O_4 or Eu_2O_3 phases, which form under oxygen excess. This mainly paramagnetic behavior is also reflected in the $M(H)$ curve (inset), in which any hysteretic behavior of EuO contributions hardly identified.

Noticeably, although the growth parameters for stoichiometric Eu(II)O and oxygen-rich Eu(II,III)O only slightly differ in the amount supplied oxygen partial pressure by about 2×10^9 Torr for the reactive Eu:O synthesis, the alteration of the chemical state and magnetic properties is tremendous. In that, the results underline the importance of carefully controlling the narrow parameter range during growth in order to stabilize stoichiometric – and ferromagnetic – Eu(II)O ultrathin films on Silicon.

Having successfully demonstrated the feasibility to synthesize ultrathin EuO films as potential magnetic spin filter tunnel barriers, consequently the next task is characterizing and optimizing the chemical state of the transport interface with Silicon. Special attention needs to be paid to the formation of metallic impurities as those can significantly decrease the spin transfer ratio across the EuO/Si interface by spin-dependent scattering processes. We therefore studied the impact of an interface passivation with the native silicon oxide SiO_2 , in order to define in a controlled manner an additional – but nonmagnetic – tunnel barrier, which as such does not alter the spin transfer efficiency.

Interface-sensitive HAXPES spectra of the EuO/Si heterostructures are depicted in Fig. 5 (a),(b). In the Si 1s spectrum (a), SiO_x contributions are observed at chemical shifts of 3.2 and 4.1 eV, which identify Si^{3+} (Si_2O_3) and Si^{4+} (SiO_2). Another component with a chemical shift to lower BE is identified as a metallic Eu silicide (EuSi_y) contribution both in the Si1s and Eu 4d spectrum in Fig. 5 (a),(b). A quantitative thickness determination of the SiO_x passivation layer and of the interfacial EuSi_y reaction layer is accomplished by consistent least squares peak fitting [31, 35, 36]. We found EuSi_y to exceed 10\AA

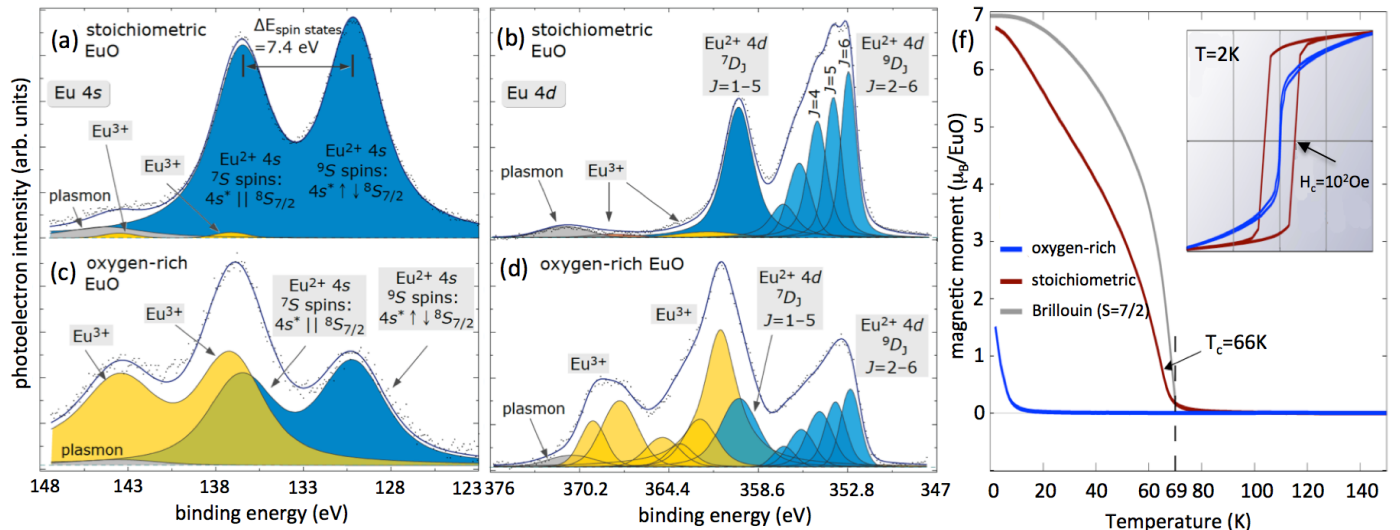


Figure 4: (color online) HAXPES spectra of 4.5 nm EuO directly grown on HF-etched Si(001) recorded at $h\nu = 4.2$ keV. Eu $4d$ and Eu $4s$ core levels are shown for (a),(b) stoichiometric Eu(II)O and (c),(d) oxygen-rich Eu(II,III)O films. (f) Magnetic properties of 4.5 nm thick EuO films grown on HF-etched Si(001) dependent on temperature $M(T)$ and (inset) field-dependent hysteresis loops $M(H)$.

thickness for flashed Si(001), however, by applying an ultrathin SiO_x interface passivation ($d_{\text{SiO}_x} = 10 - 13\text{\AA}$), the silicide formation is suppressed by 68% to $d_{\text{EuSi}_2} \leq 7.5\text{\AA}$. The optimum value for the quasi-contamination free EuO/Si interface is achieved with 13\AA SiO_x passivation, for which the silicide is diminished down to 1.8\AA , well below one monolayer of interface coverage.

Finally, we investigate how the magnetic properties of the EuO/Si heterostructures depend on the SiO_x interface passivation. Fig. 5 (c) summarizes the in-plane $M(T)$ and $M(H)$ SQUID curves with varying SiO_x thicknesses. Not surprisingly, EuO thin films on Si(001) without any SiO_x passivation show a significantly reduced magnetic moment and a $T_c \sim 10$ K, as the formation of a EuSi_y reaction layer largely destroys the EuO ferromagnetic behavior [38], as observed also by HAXPES. Applying the SiO_x interface passivation in turn clearly improves the EuO magnetic properties. The most effective interface passivation of 13\AA SiO_x yields $M_S = 5\mu_B$ and $T_C = 68$ K, close to the respective bulk values. With increasing SiO_x passivation thickness, however, structural defects and surface roughening cause an increase of the EuO coercive field of up to 180 Oe.

In summary, we have demonstrated that stabilizing high quality EuO magnetic tunnel barriers directly on Silicon is feasible by carefully controlling the narrow range of synthesis parameters. Inserting an ultrathin SiO_2 -interface passivation layer acts as a reaction barrier for the transport interface by significantly reducing silicide formation. In thus, the integration of spin filtering and conductance-matched magnetic tunnel barriers directly with Silicon may open up novel pathways for the upcoming developments in silicon spintronics.

5. Resistive Switching: HAXPEEM

In order to reduce the energy consumption of information technology, a fast high-density nonvolatile memory is needed. Among the different avenues followed is the concept of resistive switching in oxides [39] or chalcogenides [40]. The physical mechanisms underlying resistive switching include redox processes and phase changes. A particular challenge in the investigation of resistive switching phenomena is the small area where the changes take place. With a lateral resolution of a few 10 nm, energy-filtered photoemission microscopes are ideally suited to tackle this challenge. Studies in the soft x-ray regime have already contributed significantly to the understanding of the microscopic processes during electroforming in Fe-doped strontium titanate [41] and resistive switching in gallium oxide [42].

The major drawback of using soft x-rays, however, is the limited information depth of the photoemission signal. This precludes *in-operando* studies of the switching process, as most resistive switching contacts involve a vertical contact geometry with a metallic top electrode. Accessing the chemical changes in the oxide chalcogenide layer therefore requires a delamination of the top electrode – which may cause unwanted artefacts in the experiment. In order to overcome this problem we are currently developing energy-filtered hard x-ray photoemission microscopy (HAXPEEM) [12, 43]. Using photoelectrons with kinetic energies of around 5-6 keV permits access to interfaces buried below a 10 nm thick top electrode.

A result from a first HAXPEEM test experiment on a Au/Si checkerboard structure is shown in Fig. 6. We used photons with an energy of 6.5 keV delivered by the beamline P09 at PETRA-III (Hamburg). The images were acquired with a modified NanoESCA system capable of

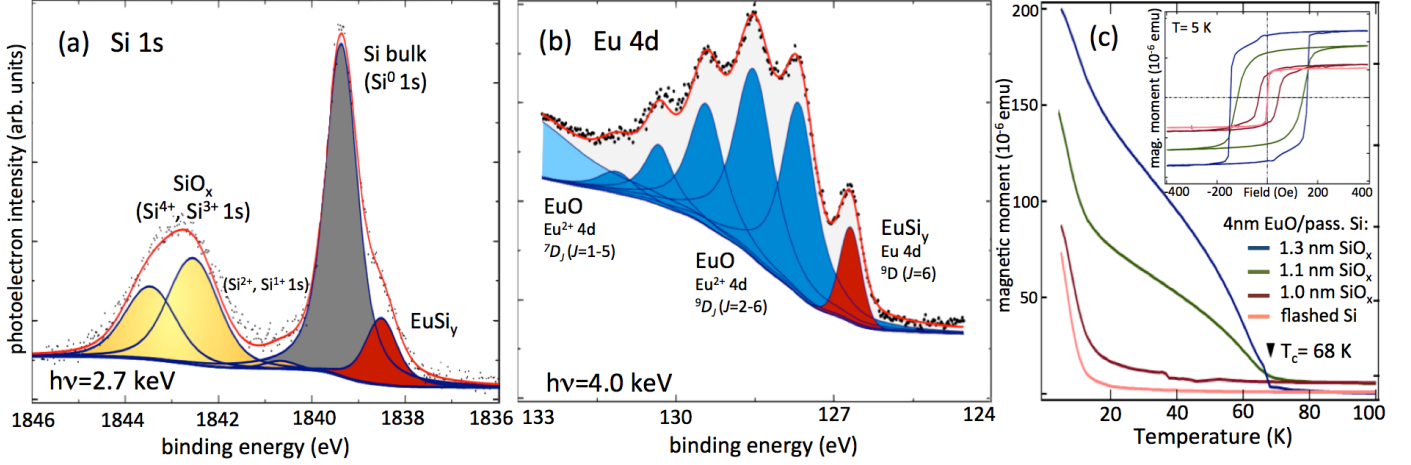


Figure 5: (color online) (a) Si 1s and (b) Eu 4d HAXPES spectra of SiO_x-passivated EuO/Si(001) samples used for quantitative peak fitting analysis. (c) Magnetic properties of EuO/Si heterostructure with different SiO_x passivation layers.

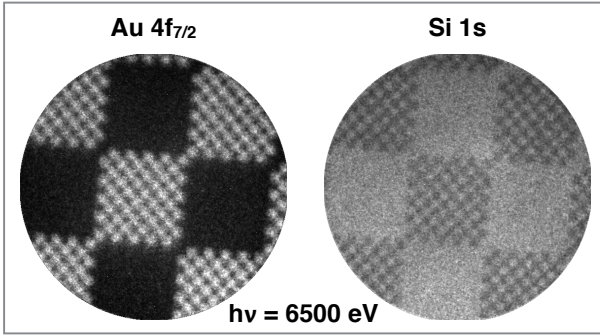


Figure 6: Hard x-ray spectromicroscopy from a test structure. The checkerboard pattern is formed by 1 μ m edge length square Au elements on Si, which are grouped into 10 μ m edge length arrays. Au 4f_{7/2} (left) and Si 1s photoemission signal (right).

energy filtering up to a electron kinetic energy of 6 keV [43]. At the Au 4f_{7/2} line the kinetic energy is about $E_{kin} \sim 6.4$ keV and the image shows a clear chemical contrast. The image recorded at the Si 1s line has an inverted contrast, but is more noisy as the respective photoemission signal is only half the size of the signal from Au. This result demonstrated that hard x-ray spectromicroscopy is possible with a lateral resolution of at least 500 nm.

In order to address the aspect of information depth we have designed a specific test sample with a wedge-shaped Cr top layer covering a sharp transition between Si and Au (Fig. 7a). The results displayed in Fig. 7b reflect the lateral distribution of the Au 3d photoemission signal at a photo excitation with $h\nu = 6550$ eV. The sharp edge separating the Si and Au regions is clearly visible. The gradual decrease of the Au 3d photoemission signal reflects the attenuation of the photoelectrons with a kinetic energy of $E_{kin} = 4342$ eV in the top Cr layer. From a modelling of this decrease we obtain an inelastic mean free path of $\lambda_{in} \approx 4.9$ nm [12].

These results demonstrate that hard x-ray spectromi-

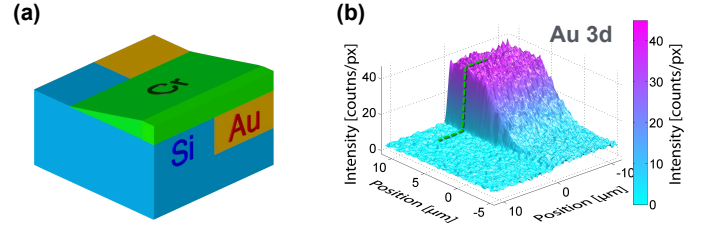


Figure 7: Hard x-ray spectromicroscopy from a wedge-shaped test structure. (a) Sample layout, thickness of Au inlay is 100 nm. The maximum thickness of the Cr top layer is 15 nm. (b) Lateral distribution of the Au 3d photoemission signal, reflecting the attenuation through the Cr overlay.

croscopy has reached a state that enables future in-operando experiments on resistive switching materials.

6. Ambient pressure XPS

Solid/gas, liquid/gas, and solid/liquid interfaces play a major role in many important areas of science and technology, e.g. in energy generation, electrochemistry, corrosion, environmental science, and information technology, yet pose experimental challenges for the investigation of their chemical and structural properties on the molecular scale. For example, the electrical double-layer has been studied for over 100 years, and yet is not fully understood [44, 45]. Characterizing such interfaces requires enhancing the signal from the narrow interfacial regions over those originating from the layers on either side of them.

We here combine standing-wave and ambient-pressure photoemission (SWAPPS) to study the regions near a solid/liquid and a liquid/gas interface, represented by a hydrated, mixed NaOH/CsOH layer on a polycrystalline hematite surface. We show that SWAPPS can determine the chemical-state resolved depth profiles of every element in the sample with

sub-nm resolution. For example, we show that the Na and Cs ion have distinctly different depth distributions. This work thus demonstrates the high future potential of SWAPPS for studying a broad range of interface phenomena.

One possibility to prepare thin liquid films is to expose the sample to precisely controlled relative humidities (RH) just below saturation ($RH = 100\%$), since the water film thickness increases rapidly as the RH approaches 100% . The challenges of this approach are three-fold: (I) The precise control of temperature and water vapor pressure in the experiment, since any small deviation will lead to rapid liquid film growth or desorption. (II) The control of the concentration and pH of the solution. While alkali halide solution films have successfully been formed by rehydrating either drop-cast or evaporated alkali halide films inside a humidity-controlled vacuum chamber [46, 47], the exact control of the concentration and pH of the film is challenging. (III) Finally, the connection of the liquid film to an external electrical circuit, which might be achieved using an approach akin to scanning probe methods to immerse an electrode into the thin solution film.

These challenges can be overcome using the so-called meniscus method, which was first introduced many decades ago by Bockris and colleagues for the determination of the dissolution of gases in porous electrodes [48], and recently been applied by some of the authors of this article for the first time to studies of liquid/solid interfaces using APXPS. The principle is shown in Fig. 2. The sample is immersed in a solution inside the measurement cell and can then be electrochemically cleaned of hydrocarbons and other contamination. When it is partially withdrawn from the solution, a meniscus will extend to a height z_1 (for neat water on a hydrophilic surface, a few mm) [49] above the bulk solution surface. Under favorable conditions and in the presence of a vapor pressure p_{vap} (which is a function of the solution temperature T_{sol}) close to saturation, a thin liquid film can be stabilized over the whole range over which the sample was originally dipped into the solution (z_2). Close to the top of the liquid film (at $\sim z_2$) parts of the liquid film are sufficiently thin to allow collection of photoelectron spectra from the liquid/solution interface. Liquid films formed in that manner have been shown to be stable for many hours. This method was used in the present experiments and is described in more detail in the Experimental section.

The last challenge that needs to be overcome in the study of liquid/solid interfaces using APXPS is enhancing the signal from the narrow interfacial region over that originating from the bulk of the liquid layer and solid substrate. To that end, some of the authors of this paper have recently introduced standing wave ambient pressure photoemission spectroscopy (SWAPPS), which is based on well-established standing wave photoemission spectroscopy, where the exciting X-ray wave field is tailored into a standing wave that is scanned through the interface of interest and thus provides much increased depth-resolution in XPS

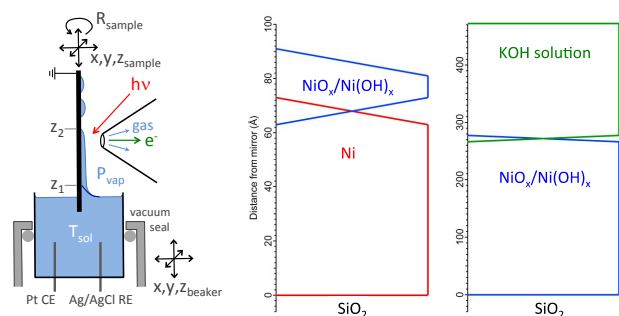


Figure 8: (color online) Soft X-ray standing wave study of a hematite sample hydrated in ambient water vapor pressure of 400 mTorr. (a) An experimental schematic of the multilayer mirror, the hematite layer, the wet layer and the humid environment. (b) Depth resolved concentration profiles of various chemical species. Adapted from [47].

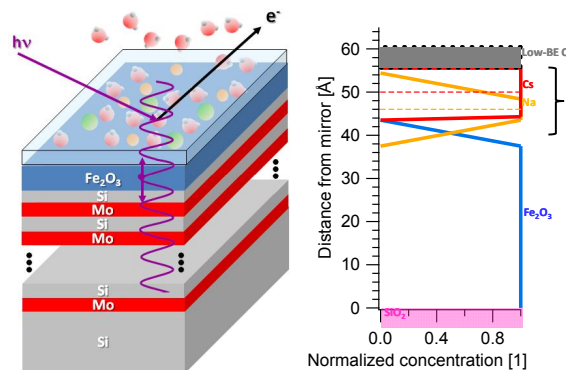


Figure 9: (color online) Hard X-ray standing wave in-operando photoemission study of nickel oxidation using a dip-stick method. (a) Schematics of the meniscus method. (b) and (c) Depth concentration profiles of various species for a dry and dipped sample, respectively. Adapted from [52].

experiments [50, 51]. The advantage of the standing wave approach is that it provides a built-in ruler, i.e., the period of the standing wave, to determine absolute depth distributions of chemical species throughout the probed volume. The combination of SWAPPS with the meniscus method for the preparation of thin liquid layers thus has the potential to provide detailed chemical information about all components of the system (bulk liquid, liquid/solid interface, bulk solid) with sub-nm resolution in the direction perpendicular to the interface, with full control over the concentration and pH of the solution, as well as the applied potentials. In the following we describe the experimental details and present a proof-of-principle investigation for the reaction of Ni immersed in a 0.1 M KOH solution under oxidizing conditions.

The last aspect deserving our attention is the soft- versus hard- x-ray excitation in standing wave ambient pressure photoemission. Reflectivity is the driving force behind the SW generation. Challenges to be overcome while increasing the excitation energy are the decreasing reflectiv-

ity, photoelectron cross-sections and lower incident angles (problematic with a finite beam size). Despite the problems, solid-liquid interface can be probed by APXPS for liquid layers of up to 10 nm thick by using multi keV excitation.

Acknowledgement

We are grateful to Prof. C. S. Fadley for the ongoing collaboration on many aspects of soft and hard x-ray photoemission. We acknowledge experimental work by C. Caspers. M.M. acknowledges financial support by the Deutsche Forschungsgemeinschaft (DFG) under Grant MU3160/1-1 and by the Helmholtz Association (HGF) under Contract No. VH-NG-811. C. M. S. acknowledges support of the DFG through the CRC 917.

References

- [1] S. Hüfner, *Photoelectron Spectroscopy* (Springer-Verlag, Berlin, 2003).
- [2] F. Reinert and S. Hüfner, *New J. Phys.* **7** (2005) 97.
- [3] C. S. Fadley, *J. Electron Spectr. Rel. Phen.* **178-179** (2010) 2.
- [4] K. Kobayashi, *Nucl. Instrum. Methods A* **601** (2009) 32.
- [5] C. S. Fadley, *J. Electron Spectr. Rel. Phen.* **190** (2013) 165.
- [6] C. S. Fadley and S. Nemšák, *J. Electron Spectr. Rel. Phen.* **195** (2014) 409.
- [7] M. Salmeron and R. Schlögl, *Surface Sci. Rep.* **63** (2008) 169.
- [8] E. J. Crumlin, H. Bluhm and Z. Liu, *J. Electron Spectr. Rel. Phen.* **190** (2013) 84.
- [9] M. Escher, N. Weber, M. Merkel, B. Krömker, D. Funnemann, S. Schmidt, F. Reinert, F. Forster, S. Hüfner, P. Bernhard, C. Zietzen, H. J. Elmers and G. Schönhense, *J. Electron Spectr. Rel. Phen.* **144-147** (2005) 1179.
- [10] C. Wiemann, M. Patt, I. P. Krug, N. B. Weber, M. Escher, M. Merkel and C. M. Schneider, *e-J. Surf. Sci. Nanotech.* **9** (2011) 395.
- [11] T. Wakita, T. Taniuchi, K. Ono, M. Suzuki, N. Kawamura, M. Takagaki, H. Miyagawa, F. Guo, T. Nakamura, T. Muro, H. Akinaga, T. Yokoya, M. Oshima and K. Kobayashi, *Jpn. J. Appl. Phys.* **45** (2006) 1886.
- [12] M. Patt, C. Wiemann, N. Weber, M. Escher, A. Gloskovskii, W. Drube, M. Merkel and C. M. Schneider, *Rev. Sci. Instrum.* **85** (2014) 113704.
- [13] L. Plucinski, J. Minár, B. C. Sell, J. Braun, H. Ebert, C. M. Schneider, and C. S. Fadley, *Phys. Rev. B* **78** (2008) 035108.
- [14] C. Papp, L. Plucinski, J. Minar, J. Braun, H. Ebert, C. M. Schneider, and C. S. Fadley, *Phys. Rev. B* **84** (2011) 045433.
- [15] J. Braun, J. Minár, S. Mankovsky, V. N. Strocov, N. B. Brookes, L. Plucinski, C. M. Schneider, C. S. Fadley, and H. Ebert, *Phys. Rev. B* **88** (2013) 205409.
- [16] S. Suga, A. Sekiyama, H. Fujiwara, Y. Nakatsu, T. Miyamachi, S. Imada, P. Baltzer, S. Niitaka, H. Takagi, K. Yoshimura, M. Yabashi, K. Tamasaku, A. Higashiyama, and T. Ishikawa, *New J. Phys.* **11** (2009) 073025.
- [17] Y. Takata, Y. Kayanuma, S. Oshima, S. Tanaka, M. Yabashi, K. Tamasaku, Y. Nishino, M. Matsunami, R. Eguchi, A. Chainani, M. Oura, T. Takeuchi, Y. Senba, H. Ohashi, S. Shin, and T. Ishikawa, *Phys. Rev. Lett.* **101** (2008) 137601.
- [18] R. Jansen *et al.*, *Semicond. Sci. Tech.* **27**, 083001 (2012)
- [19] F. Matsakura, H. Ohno and T. Dietl, in: *III-V Ferromagnetic Semiconductors*, eds. K. H. J. Buschow (Elsevier Science Publishers, Amsterdam, 2002).
- [20] Y. Ohno, D. K. Young, B. Beschoten, F. Matsukura, H. Ohno and D. D. Awschalom, *Nature (London)* **402** (1999) 790.
- [21] A. X. Gray, J. Minar, S. Ueda, P. R. Stone, Y. Yamashita, J. Fuji, J. Braun, L. Plucinski, C. M. Schneider, G. Panaccione, H. Ebert, O. D. Dubon, K. Kobayashi, and C. S. Fadley, *Nat. Mater.* **11** (2012) 957.
- [22] A. X. Gray, C. Papp, S. Ueda, B. Balke, Y. Yamashita, L. Plucinski, J. Minar, J. Braun, E. R. Ylvisaker, C. M. Schneider, W. E. Pickett, H. Ebert, K. Kobayashi, and C. S. Fadley, *Nat. Mater.* **10** (2011) 759.
- [23] K. Sato, L. Bergqvist, J. Kudrnovský, P. H. Dederichs, O. Eriksson, I. Turek, B. Sanyal, G. Bouzerar, H. Katayama-Yoshida, V. A. Dinh, T. Fukushima, H. Kizaki, and R. Zeller, *Rev. Mod. Phys.* **82** (2010) 1633.
- [24] G.-X. Miao, M. Müller, and J. S. Moodera, *Phys. Rev. Lett.* **102**, 076601 (2009)
- [25] M. Müller, G.-X. Miao, and J. S. Moodera, *Europhys. Lett.* **88**, 47006 (2009)
- [26] M. Müller, M. Luysberg, and C. M. Schneider, *Appl. Phys. Lett.* **98**, 142503 (2011)
- [27] K.J. Hubbard and D. S. Schlom, *J. Mat. Res.* **11**, 2757 (1996)
- [28] P. G. Steenken, L. H. Tjeng, I. Elfimov, G. A. Sawatzky, G. Ghiringhelli, N. B. Brookes, and D.-J. Huang, *Phys. Rev. Lett.* **88**, 047201 (2002)
- [29] R. Sutarto, S. G. Altendorf, B. Coloru, M. Moretti Sala, T. Haupricht, C. F. Chang, Z. Hu, C. Schüssler-Langeheine, N. Hollmann, H. Kierspel, H. H. Hsieh, H.-J. Lin, C. T. Chen, and L. H. Tjeng, *Phys. Rev. B* **79**, 705318 (2009)
- [30] C. Caspers, M. Müller, A. X. Gray, A. M. Kaiser, A. Gloskovskii, C. S. Fadley, W. Drube, and C. M. Schneider, *Phys. Rev. B* **84**, 205217 (2011); *physica status solidi (RRL)* **5**, 441 (2011)
- [31] C. Caspers, M. Müller, A. X. Gray, A. M. Kaiser, A. Gloskovskii, C. S. Fadley, W. Drube, and C. M. Schneider, *Phys. Rev. B* **84**, 205217 (2011); *J. Appl. Phys.* **113**, 17C505 (2013)
- [32] C. S. Fadley, *J. Electr. Spectr.* **190**, 165 (2013)
- [33] A. Gloskovskii, *J. Electron Spectrosc.* **185**, 47 (2012)
- [34] M. Gorgoi, S. Svensson, F. Schäfers, G. Öhrwall, M. Mertin, P. Bressler, O. Karis, H. Siegbahn, A. Sandell, H. Rensmo, W. Doherty, C. Jung, W. Braun, and W. Eberhardt, *Nucl. Instrum. Methods A* **601**, 48 (2009)
- [35] S. Tanuma, C. J. Powell, and D. R. Penn, *Surf. Interf. Analysis* **41**, 689 (2011)
- [36] Th. Eickhoff, V. Medicherla, and W. Drube, *J. Electron Spectrosc.* **137-140**, 85 (2004)
- [37] E.-J. Cho, S.-J. Oh, S. Imada, S. Suga, T. Suzuki, and T. Kasuya, *Phys. Rev. B* **51**, R10146 (1995); *Phys. Rev. B* **59**, R15613 (1999)
- [38] C. Caspers, Ph.D. thesis, University Duisburg-Essen (2013)
- [39] R. Waser and M. Aono, *Nat. Mater.* **6** (2007) 833.
- [40] M. Wuttig and N. Yamada, *Nat. Mater.* **6** (2007) 824.
- [41] C. Lenser, M. Patt, S. Menzel, A. Koehl, C. Wiemann, C. M. Schneider, R. Waser and R. Dittmann, *Advanced Functional Materials* **24** (2014) 4466.
- [42] Y. Aoki, C. Wiemann, V. Feyer, H.-S. Kim, C. M. Schneider, H. Ill-Yoo and M. Martin, *Nat Commun* **5** (2014).
- [43] C. Wiemann, M. Patt, S. Cramm, M. Escher, M. Merkel, A. Gloskovskii, S. Thiess, W. Drube and C. M. Schneider, *Appl. Phys. Lett.* **100** (2012) 223106.
- [44] H. Ohno, *Electrochemical Aspects of Ionic Liquids*, (John Wiley & Sons, 2011)
- [45] G. E. Brown and G. Calas, *Geochem. Perspect.* **1**, 483-742 (2012), with special discussion of the mineral-electrolyte double layer and prior standing-wave x-ray emission studies over pp. 552-557
- [46] K. Arima, P. Jiang, X. Deng, H. Bluhm and M. Salmeron, *J. Phys. Chem. C*, 2010, **114**, 14900.
- [47] S. Nemšák, A. Shavorskiy, O. Karslioglu, I. Zegkinoglou, P.K. Greene, E.C. Burks, K. Liu, A. Rattanachata, C.S. Conlon, A. Keçi, F. Salmassi, E.M. Gullikson, S.-H. Yang, H. Bluhm and C.S. Fadley, *Nat. Comm.*, 2014, **5**, 5441, doi: 10.1038/ncomms6441.
- [48] J. O'M. Bockris and B.D. Cahan, *J. Phys. Chem.*, 1969, **50**,

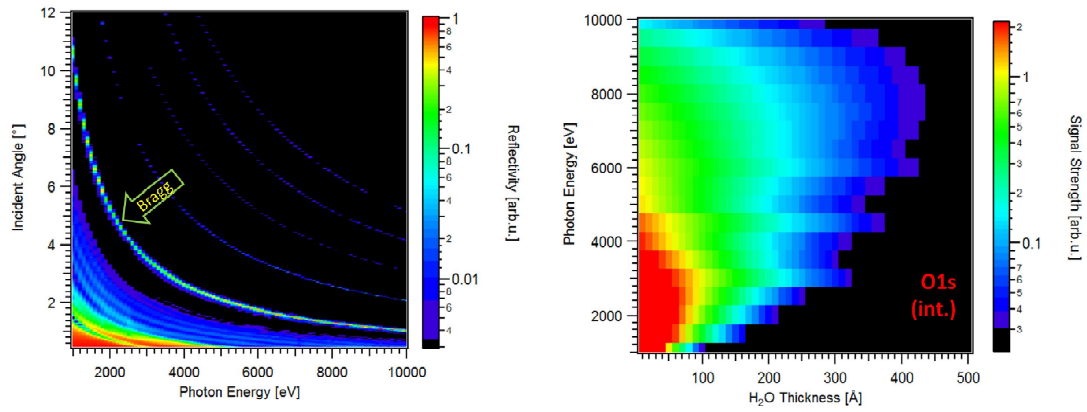


Figure 10: (color online) (a) Reflectivity dependence and (b) photoemission intensity of O1s signal originating from the solid-liquid interface as a function of photon energy.

1307.

- [49] P.-G. de Gennes, F. Brochard-Wyart, D. Quéré, *Capillarity and Wetting Phenomena*, (Springer, New York, 2004).
- [50] C.S. Fadley, *J. Electron Spectrosc. Relat. Phenom.*, 2013, **190**, 165.
- [51] A.X. Gray, *J. Electron Spectrosc. Relat. Phenom.*, 2014, **195**, 399.
- [52] O. Karslioglu, S. Nemsak, I. Zegkinoglou, A. Shavorskiy, M. Hartl, F. Salmassi, E. Gullikson, M.-L. Ng, C. Rameshan, B. Rude, D. Bianculli, A. Cordones-Hahn, S. Axnanda, E. Crumlin, P. N. Ross, C. M. Schneider, Z. Hussain, Z. Liu, C. S. Fadley and H. Bluhm, *Faraday Discuss.* (in print, DOI: 10.1039/C5FD00003C).